

# Low-temperature thermal transport in moiré superlattices

Lukas P. A. Krisna,\* Takuto Kawakami, and Mikito Koshino

*Department of Physics, Osaka University, Toyonaka, Osaka 560-0043, Japan*

(Dated: May 2, 2024)

We calculate the thermal conductivity of various moiré bilayer systems using a continuum approach and the semiclassical transport theory. When the twist angle is close to 0, we observe a significant reduction of thermal conductivity in a particular low-temperature regime. This reduction is attributed to a moiré-induced reconstruction of acoustic phonon bands and associated decrease of the group velocity. Conversely, in the zero temperature limit, the thermal conductivity is enhanced by moiré effect, surpassing the original values in non-moiré counterparts. These changes result in a characteristic temperature dependence which deviates from the quadratic behavior in intrinsic two-dimensional systems.

## I. INTRODUCTION

In recent years, significant advancements have emerged in the field of two-dimensional (2D) moiré materials, following the discovery of various exotic phenomena in twisted bilayer systems [1–7]. The electronic structure of these materials are strongly modulated by the emerged superlattice of the long-range periodic pattern [8–16]. In a similar manner, moiré patterns also have notable influence on the lattice vibration. In twisted systems, the interlayer moiré potential folds the original monolayer phonon bands into the superlattice Brillouin zone [17–22]. When the moiré superlattice period is much greater than the atomic scale, spontaneous lattice relaxation renormalizes the phonon modes [23–33], and the acoustic bands are reconstructed with notable band flattening and the appearance of spectral gaps [23–25]. These changes are expected to have significant influence in the thermal transport phenomena where acoustic phonons are the dominant heat carrier.

Heat transport in 2D materials has attracted notable interest because of its superiority and its sensitivity to heterostructuring. For example, the high thermal conductivity of suspended graphene [34–37] is significantly decreased in the presence of substrate or other layer due to strong scattering of flexural phonons [38–44]. Meanwhile, experimental measurements demonstrated further suppression when rotationally stacked graphene layers [45, 46]. Theoretical simulations showed that such a thermal conductivity reduction by a twist can be caused by the enhancement of anharmonic phonon scattering and the redistribution of phonons to higher frequencies [47–51]. While all these simulations assumed the room temperature and above, the effect of moiré-induced phonon band reconstruction on the thermal properties is expected to be relevant in the low temperature regime, and it remains unknown.

In this paper, we calculate the thermal conductivity of various representative twisted bilayer systems, including twisted bilayer graphene (TBG) and twisted

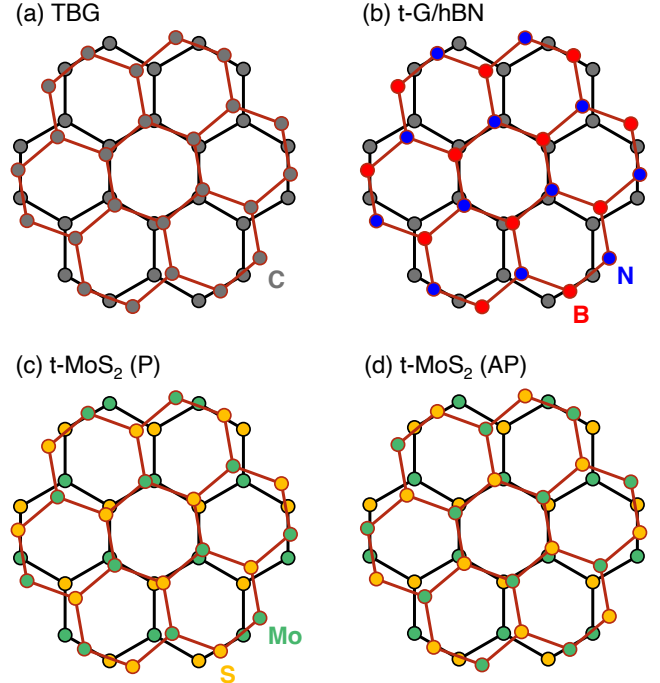


Figure 1. Top view of atomic structures of (a) twisted bilayer graphene (TBG), (b) twisted graphene/hBN (t-G/hBN), (c) parallel-stacked twisted bilayer MoS<sub>2</sub> (t-MoS<sub>2</sub> (P)), and (d) antiparallel-stacked twisted bilayer MoS<sub>2</sub> (t-MoS<sub>2</sub> (AP)). Each yellow circle in (c) and (d) represent overlapped double S atoms at different perpendicular positions.

graphene/hexagonal boron nitride (t-G/hBN), and also twisted bilayer molybdenum disulfide (t-MoS<sub>2</sub>) in both parallel (P) and antiparallel (AP) stacking arrangement [Fig. 1]. Here, we obtain the phonon band structure by the continuum approach, which has been extensively utilized to describe lattice relaxation and the formation of superlattice mini-bands in the phonon dispersion relation [23–25, 52]. Then we calculate the thermal conductivity using a semiclassical transport theory in the low temperature regime assuming a constant mean free path. We demonstrate that the flattening of the low-energy phonons bands leads to a significant suppression

\* lukas@qp.phys.sci.osaka-u.ac.jp

of thermal conductivity up to 40%, resulting in a characteristic deviation from the generic quadratic temperature dependence of thermal conductivity in two-dimensional system.

This paper is organized as follows. In Sec. II, we introduce the continuum method to describe long-wavelength phonons, and the formulation of semiclassical transport to calculate the thermal conductivity in the low-temperature regime. In Sec. III, we present and discuss the calculated phonon dispersion of each system and the corresponding thermal conductivity. Finally, a brief conclusion is given in Sec. IV.

## II. METHODS

### A. Lattice geometry

We consider a twisted bilayer system composed of two honeycomb lattice layers with generally different lattice constants,  $a$  and  $a'$ , as illustrated in Fig. 2(a). The layer 2 is stacked on top of the layer 1 with relative rotation angle  $\theta$  around a common honeycomb center. We label the sublattices of layer 1 by A and B, and that of layer 2 by A' and B' as in Fig. 2(a). The primitive lattice vectors of layer 1 are defined as  $\mathbf{a}_1 = a(1, 0)$  and  $\mathbf{a}_2 = a(1/2, \sqrt{3}/2)$ , and those of layer 2 are given by  $\mathbf{a}'_i = \hat{M}\hat{R}(\theta)\mathbf{a}_i$  ( $i = 1, 2$ ), with rotation matrix  $\hat{R}(\theta)$  and isotropic expansion matrix  $\hat{M} = (1 + \varepsilon)\hat{I}$  where  $\varepsilon = (a' - a)/a$ . The corresponding reciprocal lattice vectors for layer 1 and 2 are given by  $\mathbf{b}_i$  and  $\mathbf{b}'_i$ , respectively, which satisfy  $\mathbf{a}_i \cdot \mathbf{b}_j = \mathbf{a}'_i \cdot \mathbf{b}'_j = 2\pi\delta_{ij}$ . A long-range moiré interference pattern appears due to a slight mismatch from a small difference in lattice constant or small twist angle. The reciprocal lattice vectors of the pattern are given by  $\mathbf{G}_i^M = \mathbf{b}_i - \mathbf{b}'_i$ , while the corresponding real-space lattice vectors are obtained from the condition  $\mathbf{L}_i^M \cdot \mathbf{G}_j^M = 2\pi\delta_{ij}$ . The moiré period  $L_M = |\mathbf{L}_i^M|$  can be expressed as

$$L_M = a \frac{1 + \varepsilon}{\sqrt{\varepsilon^2 + 2(1 + \varepsilon)(1 - \cos \theta)}}. \quad (1)$$

For honeycomb lattice components, we take graphene, hexagonal boron nitride, and molybdenum disulfide with lattice constant of  $a \approx 0.246$  nm, 0.2504 nm, and 0.317 nm, respectively. In this paper, we consider twisted bilayer graphene (TBG) and twisted bilayer molybdenum disulfide (t-MoS<sub>2</sub>) as examples of homo-bilayer ( $\varepsilon = 1$ ) and also twisted graphene/hexagonal boron nitride (t-G/hBN) as a heterobilayer ( $\varepsilon \neq 1$ ). In Fig. 2(c), we illustrate the formation of moiré superlattice in t-G/hBN with  $\theta = 1.25^\circ$  where a lattice constant difference  $\varepsilon \approx 1.8\%$  and the twist angle produce a moiré pattern of  $L_M = |\mathbf{L}_i^M| \approx 8.8$  nm.

Across the moiré pattern, the local stacking structure changes smoothly at the atomic scale. At a given position  $\mathbf{r}$ , it is characterized by the phase difference  $(\varphi_1, \varphi_2)$

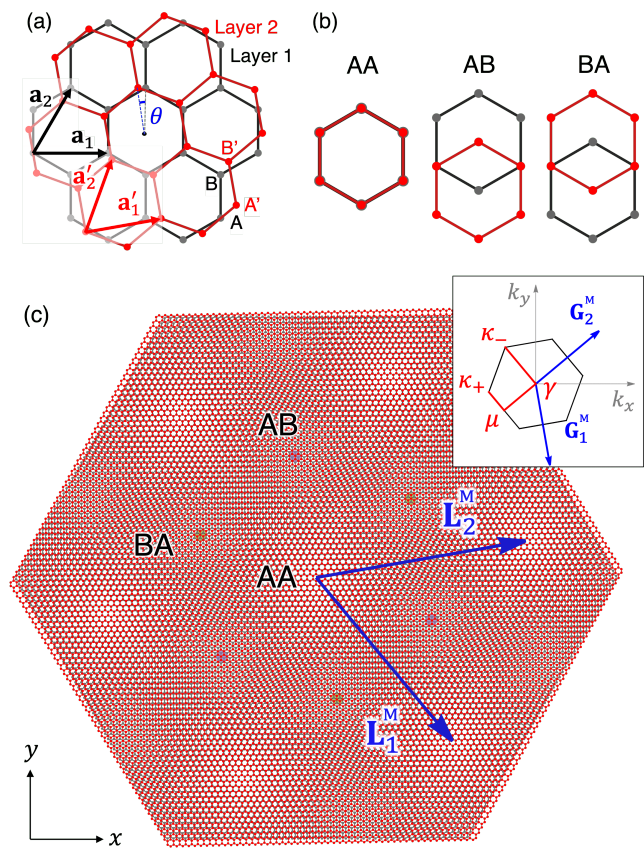


Figure 2. (a) Schematic diagram of a twisted bilayer system. (b) Three local stacking structures AA, AB, and BA. (c) Non-relaxed atomic structure of t-G/hBN with  $\theta = 1.25^\circ$ . The inset shows the first moiré Brillouin zone.

defined as

$$\varphi_j(\mathbf{r}) = (\mathbf{b}_j - \mathbf{b}'_j) \cdot \mathbf{r} = \mathbf{G}_j^M \cdot \mathbf{r}. \quad (2)$$

For example,  $(\varphi_1, \varphi_2) = (0, 0)$ ,  $(2\pi/3, 2\pi/3)$  and  $(4\pi/3, 4\pi/3)$  correspond to AA (complete alignment of the honeycomb lattices), AB (B'-site of layer 2 on top of A-site of layer 1), and BA (A'-site of layer 2 on top of B-site of layer 1), respectively [Fig. 2(b)]. We note that, when stacking two monolayers with different sublattice atoms, e.g., t-MoS<sub>2</sub>, there are two possible stacking configuration, parallel (P) and antiparallel (AP), which are related by  $180^\circ$  rotation of layer 1. In the parallel stacking, the two layers have identical atoms at A and A' (B and B'), whereas in the antiparallel stacking, the two layers have different atoms on the same sublattice sites.

### B. Continuum model

We describe the in-plane lattice vibration in the twisted bilayer systems using a continuum approach [23–25]. In this framework, we consider a smoothly-varying displacement field  $\mathbf{u}^{(l)}(\mathbf{r}, t)$  at layer  $l$  ( $l = 1, 2$ ), which represents the shift of the atom at  $\mathbf{r}$  in the original rigid

lattice, and express the Lagrangian as a functional of  $\mathbf{u}^{(l)}(\mathbf{r}, t)$ . Here we only consider the in-plane atomic displacement  $\mathbf{u}^{(l)} = (u_x^{(l)}, u_y^{(l)})$  neglecting the out-of-plane component. In the presence of the lattice distortion, the phase difference [Eq. (2)] is modified as

$$\varphi_j(\mathbf{r}, t) = \mathbf{G}_j^M \cdot [\mathbf{r} - \mathbf{u}^+(\mathbf{r}, t)/2] + \bar{\mathbf{b}}_j \cdot \mathbf{u}^-(\mathbf{r}, t), \quad (3)$$

where we have defined the (interlayer) symmetric and antisymmetric displacements  $\mathbf{u}^\pm = \mathbf{u}^{(2)} \pm \mathbf{u}^{(1)}$ , and  $\bar{\mathbf{b}}_j = (\mathbf{b}_j + \mathbf{b}'_j)/2$ .

The Lagrangian is explicitly written as  $L = T - (U_E + U_B)$ , where  $T$  is the kinetic energy,  $U_E$  is the elastic energy, and  $U_B$  is the interlayer binding energy. The  $U_B$  is defined by

$$U_B = \int V[\varphi_1(\mathbf{r}, t), \varphi_2(\mathbf{r}, t)] d^2\mathbf{r}, \quad (4)$$

where  $V[\varphi_1, \varphi_2]$  is the interlayer binding energy per area of the non-rotated bilayer with an interlayer registry specified by  $\varphi_i$ . By  $120^\circ$  symmetry of the system, it should be written within the lowest harmonics as

$$V[\varphi_1, \varphi_2] = \sum_{j=1}^3 2V_0 \cos(\varphi_j + \varphi_0), \quad (5)$$

where  $\varphi_3 = -\varphi_1 - \varphi_2$ , and the constant energy offset is neglected. The energy of AA, AB, and BA bilayer stacking is then given by  $V_{AA} = 6V_0 \cos(\varphi_0)$ ,  $V_{AB} = 6V_0 \cos(\varphi_0 + \frac{2}{3}\pi)$ , and  $V_{BA} = 6V_0 \cos(\varphi_0 - \frac{2}{3}\pi)$ . Here we obtain the parameters  $(V_0, \varphi_0)$  from the relative values of  $V_{AA}$ ,  $V_{AB}$ , and  $V_{BA}$  found in the literature. Table I lists the values of  $(V_0, \varphi_0)$  and the corresponding  $(V_{AA}, V_{AB}, V_{BA})$  for the considered systems in this paper.

The energy cost for intralayer distortion,  $U_E$  is given by standard expression of elastic theory [58, 59],

$$U_E = \sum_{l=1}^2 \frac{1}{2} \int (\lambda^{(l)} + \mu^{(l)}) \left( u_{xx}^{(l)} + u_{yy}^{(l)} \right)^2 + \mu^{(l)} \left[ \left( u_{xx}^{(l)} - u_{yy}^{(l)} \right)^2 + 4 \left( u_{xy}^{(l)} \right)^2 \right] d^2\mathbf{r}, \quad (6)$$

where  $u_{ij}^{(l)} = (\partial_i u_j^{(l)} + \partial_j u_i^{(l)})/2$  is the strain tensor, and  $\lambda^{(l)}$  and  $\mu^{(l)}$  are the Lamé parameters for layer  $l$  which are given in Table II. The kinetic energy is expressed as

$$T = \sum_{l=1}^2 \int \frac{1}{2} \rho^{(l)} \left( \dot{u}_x^{(l)2} + \dot{u}_y^{(l)2} \right) d^2\mathbf{r}, \quad (7)$$

where  $\rho^{(l)}$  is the mass density of layer  $l$ . The mass density for graphene, hBN, and MoS<sub>2</sub> are given in Table II. For the layer convenience, we define averaged materials parameters

$$\begin{aligned} \lambda &= \frac{1}{2}(\lambda^{(1)} + \lambda^{(2)}), & \mu &= \frac{1}{2}(\mu^{(1)} + \mu^{(2)}), \\ \rho &= \frac{1}{2}(\rho^{(1)} + \rho^{(2)}). \end{aligned} \quad (8)$$

The equation of motion is given by the Euler-Lagrange equation for the Lagrangian  $L$ . It can be effectively decoupled in terms of the symmetric and the antisymmetric components  $\mathbf{u}^\pm$  [23, 25]. The hybridization between  $\mathbf{u}^\pm$  is caused by the difference of the parameters  $\rho^{(l)}, \lambda^{(l)}, \mu^{(l)}$  between two layers, and therefore it is present only in heterobilayers [25]. In bilayers composed of materials with closely matched physical parameters, such as t-G/hBN, these effects are minor and will be neglected in the following argument.

The effect of the moiré interlayer coupling is much more significant in the antisymmetric part  $\mathbf{u}^-$  than in the symmetric part  $\mathbf{u}^+$ , as the phase difference  $\varphi_i$  in Eq. (3) is more sensitive to  $\mathbf{u}^-$  because of  $|\bar{\mathbf{b}}_j| \gg |\mathbf{G}_j^M|$  [25]. By neglecting  $\mathbf{u}^+$  in  $\varphi_i$ , the equation of motion for  $\mathbf{u}^+$  becomes equivalent to that for the single-layer honeycomb lattice with the averaged parameters of Eq. (8). As a result, the symmetric phonon modes are simply represented by the longitudinal (LA) and transverse (TA) acoustic modes with phonon velocity

$$v_L = \sqrt{\frac{\lambda + 2\mu}{\rho}} \quad \text{and} \quad v_T = \sqrt{\frac{\mu}{\rho}}, \quad (9)$$

respectively.

For the antisymmetric part  $\mathbf{u}^-$ , we consider the solution for in the form of

$$\mathbf{u}^-(\mathbf{r}, t) = \mathbf{u}_0^-(\mathbf{r}) + \delta\mathbf{u}^-(\mathbf{r}, t), \quad (10)$$

where  $\mathbf{u}_0^-(\mathbf{r})$  gives the relaxed state to minimize  $U_B + U_E$  and  $\delta\mathbf{u}^-(\mathbf{r}, t)$  is a small vibration around  $\mathbf{u}_0^-$ . The relaxed displacement field  $\mathbf{u}_0^-(\mathbf{r})$  is obtained by self-consistent iteration [59]. Figure 3 presents contour plots of the interlayer binding energy in the relaxed state for the considered moiré systems. Each system exhibits a characteristic domain pattern, which is determined by relative stabilities among AA, AB and BA stacking configurations (Table I). In TBG [Fig. 3(a)] and parallel t-MoS<sub>2</sub> [Fig. 3(c)], the relaxed structure reveals a triangular pattern comprising AB and BA stacking regions, indicative of the energetic equivalence between these configurations [59, 62]. In t-G/hBN [Fig. 3(b)], on the other hand, only the AB stacking dominates in the relaxed structure as it is the only structure with the lowest energy, resulting in a honeycomb domain pattern [55, 63]. The antiparallel t-MoS<sub>2</sub> [Fig. 3(d)] exhibits a honeycomb structure reminiscent of t-G/hBN, albeit with a distortion of the hexagonal domains into triangles. This distortion arises from the relatively small energy difference between the most stable AA stacking and the second stable AB stacking (see, Table I), resulting in a significant broadening of domain walls around the AB position [56, 57].

The vibration modes around the relaxed structure can be obtained as follows. We define the Fourier transform

Table I. Parameters for interlayer binding energy,  $(V_0, \varphi_0)$ , and the corresponding  $(V_{AA}, V_{AB}, V_{BA})$  for the considered systems in this paper. Note that the origin of interlayer binding energy is arbitrary.

|                                      | $V_0$ (eV/nm <sup>2</sup> ) | $\varphi_0$ | $V_{AA}$ (eV/nm <sup>2</sup> ) | $V_{AB}$ (eV/nm <sup>2</sup> ) | $V_{BA}$ (eV/nm <sup>2</sup> ) |
|--------------------------------------|-----------------------------|-------------|--------------------------------|--------------------------------|--------------------------------|
| TBG <sup>a</sup>                     | 0.160                       | 0           | 0.961                          | -0.481                         | -0.481                         |
| t-G/hBN <sup>b</sup>                 | 0.202                       | 0.956       | 0.700                          | -1.208                         | 0.509                          |
| t-MoS <sub>2</sub> (P) <sup>c</sup>  | 0.0889                      | 0           | 0.533                          | -0.267                         | -0.267                         |
| t-MoS <sub>2</sub> (AP) <sup>c</sup> | -0.0801                     | -0.805      | -0.333                         | -0.133                         | 0.467                          |

<sup>a</sup> Ref. [53, 54]

<sup>b</sup> Ref. [55]

<sup>c</sup> Ref. [56, 57]

Table II. Lamé parameter and mass density used in the calculation.

|                               | $\lambda$ (eV/Å <sup>2</sup> ) | $\mu$ (eV/Å <sup>2</sup> ) | $\rho$ (10 <sup>-8</sup> g/cm <sup>2</sup> ) |
|-------------------------------|--------------------------------|----------------------------|--|
| Graphene <sup>a</sup>         | 3.25                           | 9.57                       | 7.61   |
| hBN <sup>b</sup>              | 3.5                            | 7.8                        | 7.59   |
| MoS <sub>2</sub> <sup>c</sup> | 4.23                           | 4.23                       | 30.5   |

<sup>a</sup> Ref. [16, 60]

<sup>b</sup> Ref. [16, 61]

<sup>c</sup> Ref. [56, 57]

of  $\mathbf{u}_0^-(\mathbf{r})$  and  $\delta\mathbf{u}^-(\mathbf{r}, t)$  as,

$$\mathbf{u}_0^-(\mathbf{r}) = \sum_{\mathbf{G}} \mathbf{u}_{0,\mathbf{G}}^- e^{i\mathbf{G}\cdot\mathbf{r}}, \quad (11)$$

$$\delta\mathbf{u}^-(\mathbf{r}, t) = \frac{1}{\sqrt{S}} \sum_{\mathbf{G}} \sum_{\mathbf{q}} \delta\mathbf{u}_{\mathbf{q}+\mathbf{G}}^-(t) e^{i(\mathbf{q}+\mathbf{G})\cdot\mathbf{r}}, \quad (12)$$

where  $\mathbf{G} = m\mathbf{G}_1^M + n\mathbf{G}_2^M$  are the moiré reciprocal lattice vectors,  $\mathbf{q}$  is the wave vector within MBZ, and  $S$  is the system's total area as normalization factor. The equation of motion in the momentum-space is then given as

$$\frac{\rho}{2} \frac{d^2}{dt^2} \delta\mathbf{u}_{\mathbf{q}+\mathbf{G}}^- = - \sum_{\mathbf{G}'} \hat{D}_{\mathbf{q}}(\mathbf{G}, \mathbf{G}') \delta\mathbf{u}_{\mathbf{q}+\mathbf{G}'}^-, \quad (13)$$

where

$$\hat{D}_{\mathbf{q}}(\mathbf{G}, \mathbf{G}') = (1/2)\hat{K}_{\mathbf{q}+\mathbf{G}}\delta_{\mathbf{G},\mathbf{G}'} + \hat{V}_{\mathbf{G}'-\mathbf{G}} \quad (14)$$

is the dynamical matrix. The matrix  $\hat{K}$  is defined as

$$\hat{K}_{\mathbf{q}} = \begin{pmatrix} (\lambda + 2\mu)q_x^2 + \mu q_y^2 & (\lambda + \mu)q_x q_y \\ (\lambda + \mu)q_x q_y & (\lambda + 2\mu)q_y^2 + \mu q_x^2 \end{pmatrix}, \quad (15)$$

and the matrix  $\hat{V}$  is defined as

$$\hat{V}_{\mathbf{G}} = -2V_0 \sum_{j=1}^3 h_{\mathbf{G}}^j \begin{pmatrix} \bar{b}_{j,x}\bar{b}_{j,x} & \bar{b}_{j,x}\bar{b}_{j,y} \\ \bar{b}_{j,y}\bar{b}_{j,x} & \bar{b}_{j,y}\bar{b}_{j,y} \end{pmatrix}, \quad (16)$$

with

$$\cos[\mathbf{G}_j^M \cdot \mathbf{r} + \bar{\mathbf{b}}_j \cdot \mathbf{u}_0^-(\mathbf{r}) + \varphi_0] = \sum_{\mathbf{G}} h_{\mathbf{G}}^j e^{i\mathbf{G}\cdot\mathbf{r}}. \quad (17)$$

Equation (13) is solved by diagonalizing the dynamical matrix  $\hat{D}_{\mathbf{q}}$  to obtain the phonon frequency  $\omega_{n,\mathbf{q}}$  of mode  $n$  at  $\mathbf{q}$ . In solving this, we take sufficient cut-off in the reciprocal space, so that the result converges.

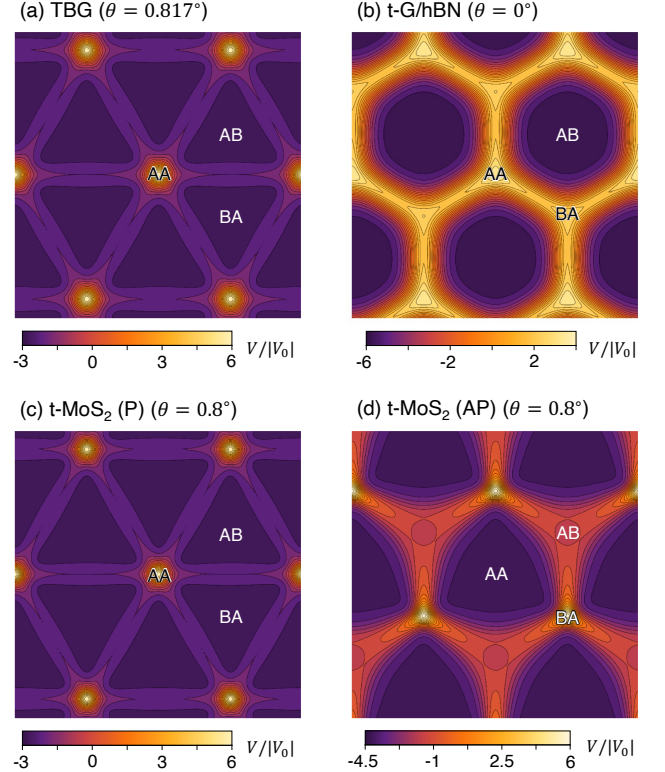


Figure 3. Contour plot of the interlayer binding energy  $V(\mathbf{r})$  in the relaxed structure of (a) 0.817° TBG, (b) 0° t-G/hBN, (c) 0.8° t-MoS<sub>2</sub> (P), and (d) 0.8° t-MoS<sub>2</sub> (AP).

### C. Thermal transport theory

Based on linearized Boltzmann transport theory with relaxation time approximation [64], thermal conductivity of 2D isotropic material can be expressed as

$$\kappa = \frac{1}{S} \sum_{n,\mathbf{q}} \frac{1}{2} v_{n,\mathbf{q}}^2 \tau_{n,\mathbf{q}} \hbar \omega_{n,\mathbf{q}} \frac{\partial f_0(\omega_{n,\mathbf{q}})}{\partial T}, \quad (18)$$

where  $S$  is the total area of the system,  $f_0(\omega) = 1/[\exp(\hbar\omega/k_B T) - 1]$  is the Bose-Einstein distribution function,  $v_{n,\mathbf{q}} = |\nabla_{\mathbf{q}} \omega_{n,\mathbf{q}}|$  is the phonon velocity,  $\tau_{n,\mathbf{q}}$  is the relaxation time, and the summation is taken over all of the mode index  $n$  and wave vector  $\mathbf{q}$ . Here, we

note that the isotropic behavior is a consequence of the three-fold rotation symmetry.

The relaxation time,  $\tau_{n,\mathbf{q}}$ , describes various scattering mechanisms that limit the mean free path of the phonon which is defined as  $\Lambda_{n,\mathbf{q}} \equiv \tau_{n,\mathbf{q}}v_{n,\mathbf{q}}$ . At low temperature, scattering due to geometric boundary is the dominant scattering mechanism and the mean free path no longer depends on the phonons frequency and wavelength, i.e.,  $\Lambda_{n,\mathbf{q}} = \Lambda$  (constant) [64]. For example, in graphitic systems,  $\Lambda$  is determined from the size and shape of the sample or the grain boundaries, and it well describes the thermal conductivity for up to 100 K [65–67]. In moiré systems, the superlattice period is generally observed to be varying across a single sample [68, 69] and this would disrupt the propagation of phonon modes [70]. In such a case,  $\Lambda$  can be regarded as a typical length where the moiré pattern remains uniform. Henceforth, we treat  $\Lambda$  as a phenomenological constant to be determined from direct measurements. The thermal conductivity is then entirely governed by the harmonic properties, and it can be written as

$$\kappa = \frac{\Lambda}{2} \int_0^\infty \tilde{n}(\omega) C(\omega, T) d\omega, \quad (19)$$

where velocity-weighted density of states (VDOS)  $\tilde{n}$  is defined as

$$\tilde{n}(\omega) = \frac{1}{S} \sum_{n,\mathbf{q}} \delta(\omega - \omega_{n,\mathbf{q}}) v_{n,\mathbf{q}} \quad (20)$$

and spectral heat capacity  $C$  is defined as

$$C(\omega, T) = \hbar\omega \frac{\partial f_0(\omega)}{\partial T} = k_B \left[ \frac{\beta\hbar\omega/2}{\sinh(\beta\hbar\omega/2)} \right]^2, \quad (21)$$

where  $\beta = 1/(k_B T)$ . In Eq. (19),  $\tilde{n}(\omega)$  contains all information regarding the phonon dispersion while  $C(\omega, T)$  acts as a weight function. The function  $C(\omega, T)$  is plotted in Fig. 4; it equals to  $k_B$  when  $\omega = 0$ , and decays exponentially for  $\hbar\omega \gtrsim 2k_B T$ . In general, the summation over mode index  $n$  would include both in-plane and out-of-plane (flexural) phonon modes. However, scattering due to substrate or other layers significantly reduces the mean free path of the flexural mode [39–44], hence, its contribution to thermal conductivity especially at low temperatures [38]. Hereafter, we will focus only on the in-plane modes contribution in the thermal conductivity.

Since only the antisymmetric phonon modes are strongly affected by the interlayer moiré potential, it is useful to write  $\kappa$  and  $\tilde{n}$  in terms of the symmetric and antisymmetric components

$$\kappa = \kappa^+ + \kappa^-, \quad \tilde{n} = \tilde{n}^+ + \tilde{n}^-, \quad (22)$$

which takes the contribution from the symmetric (+) and antisymmetric (−) phonon modes separately. In the absence of the interlayer moiré coupling (i.e., two indepen-

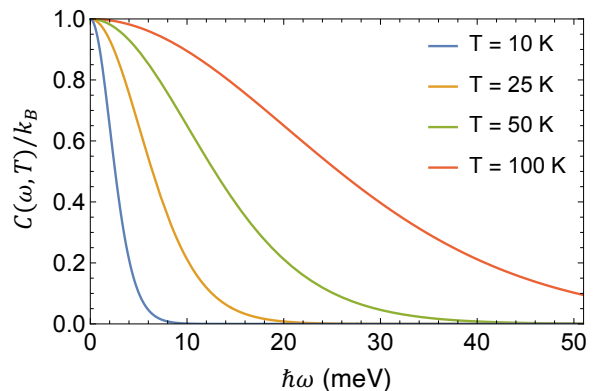


Figure 4. Plot of the spectral heat capacity function  $C(\omega, T)$  [Eq. (21)] as a function of phonon energy at different temperatures.

dent monolayers), they are given as

$$\tilde{n}_{\text{NC}}^+ = \tilde{n}_{\text{NC}}^- = \frac{1}{2} \tilde{n}_{\text{NC}} = \frac{\omega}{2\pi\bar{v}}, \quad (23)$$

$$\kappa_{\text{NC}}^+ = \kappa_{\text{NC}}^- = \frac{1}{2} \kappa_{\text{NC}} = \frac{3\Lambda\zeta(3)}{2\pi\hbar^2\bar{v}} k_B^3 T^2, \quad (24)$$

where  $\bar{v}^{-1} = v_{\text{L}}^{-1} + v_{\text{T}}^{-1}$ ,  $\zeta(n)$  is the Riemann zeta function, and NC stands for ‘non-coupled’. Here, we note that we have neglected the out-of-plane (flexural) phonon modes in the calculation of thermal conductivity. The quadratic temperature dependence of the thermal conductivity is a characteristic of linear acoustic phonon-dominated thermal transport of 2D systems in the low-temperature regime [38].

### III. RESULTS AND DISCUSSION

#### A. TBG and t-G/hBN

Figure 5 shows the calculated band dispersion and density of states for antisymmetric phonon modes in TBG with  $\theta = 5^\circ$ ,  $2.65^\circ$  and  $0.817^\circ$ . Figure 6 presents similar plots for t-G/hBN with  $\theta = 5^\circ$ ,  $3^\circ$ , and  $0^\circ$ . The phonon dispersion is plotted along the high-symmetry line in the moiré Brillouin zone (MBZ) as illustrated in Fig. 2(c). In each panel, the red-dashed line indicate the dispersion (only the lowest two branches shown) and the density of states in the non-coupled case. Here we can see that the interlayer coupling significantly modifies the band structure of the antisymmetric modes in the energy range below  $\sim 20$  meV. This reconstruction is characterized by sharp peaks in the density of states which results from the flattening of superlattice phonon bands [23–25, 32]. As the twist angle is reduced towards 0, the number of sharp peaks increases dramatically. On the other hand, the phonon bands of the symmetric phonon modes are not affected by the moiré interlayer coupling, hence they are equivalent to those of the non-coupled case (red-dashed lines).

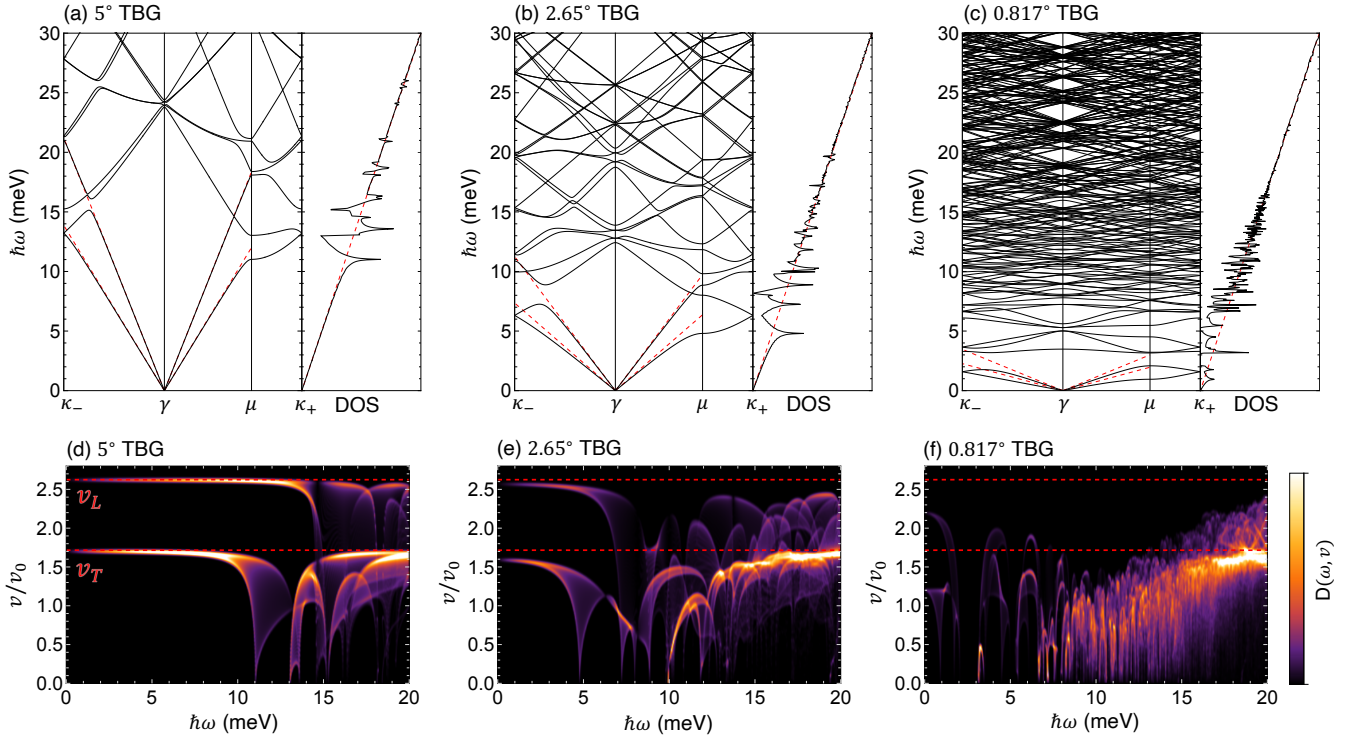


Figure 5. Band structure of the interlayer antisymmetric phonon modes (black line) and the symmetric modes (red-dashed line) for (a)  $5^\circ$ , (b)  $2.65^\circ$ , (c)  $0.817^\circ$  TBG. The right panel plots the density of states. (d)-(f) Corresponding plots for  $D(\omega, v)$ , the density of states on the frequency-velocity space [see, Eq. (25)].

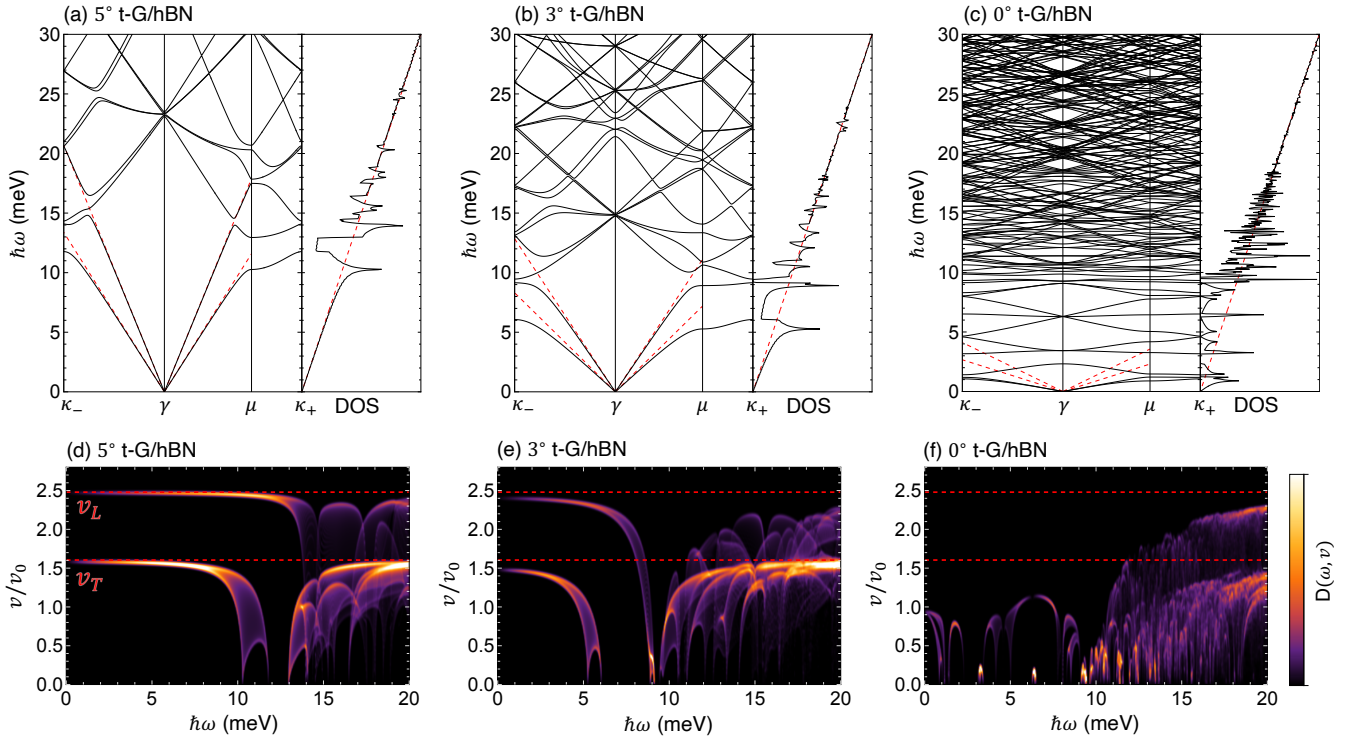


Figure 6. Plots of the band structure and  $D(\omega, v)$  similar to Fig. 5, for t-G/hBN with  $\theta = 5^\circ, 3^\circ, 0^\circ$ .

To provide a more comprehensive understanding of the band flattening effects, we present two-dimensional density maps in Fig. 5(d)-(f) and Fig. 6(d)-(f), which plot the distribution of antisymmetric phonon modes on a space of frequency and velocity, or

$$D(\omega, v) = \sum_{n, \mathbf{q}} \delta(\omega - \omega_{n, \mathbf{q}}) \delta(v - v_{n, \mathbf{q}}). \quad (25)$$

In each panel, the vertical axis is scaled by a factor of

$$v_0 = \sqrt{\lambda/\rho} \quad (26)$$

and the color brightness is a linear scale of  $D(\omega, v)$ . The horizontal red-dashed lines correspond to the velocity of the TA ( $v_T$ ) and LA ( $v_L$ ) phonons of a single layer [Eq. (9)]. Here, the flattening of phonon bands can be immediately seen as a distribution of phonon modes below  $v_T$  and  $v_L$ . In  $0.817^\circ$  TBG [Fig. 5(f)] and  $0^\circ$  t-G/hBN [Fig. 6(f)], particularly, the signals in  $\hbar\omega < 15$  meV predominantly falls below the line of  $v_T$ , i.e., nearly all of the low-energy antisymmetric phonons become slower than the original acoustic phonons in its non-moiré counterpart. Note that the distribution of symmetric phonon states (not shown) sticks to the  $v_L$  and  $v_T$  lines, where the intensity increases linearly with energy.

Figure 7(a) and (b) show  $\tilde{n}^-(\omega)$  (the VDOS of the antisymmetric phonon modes) of TBG and t-G/hBN, respectively, with various small twist angles. The effect of the moiré coupling is observed as a difference from a black-dashed line, which represents  $\tilde{n}_{\text{NC}}^+ = \tilde{n}_{\text{NC}}^- \propto \omega$  [Eq. (23)]. While VDOS is proportional to both phonon density of states and velocity, we find that the reduction of phonon velocity is more significant than the sharpening of density of states, leading to a suppression of  $\tilde{n}^-$  over a wide range of phonon frequency. We also find that the linear behavior of  $\tilde{n}^-$  remains in the low frequency region, which corresponds to the linear dispersion in the the lowest moiré phonon band in  $\omega < \omega_{\text{edge}} \approx 2\pi v_0/L_M$ . For the symmetric phonon modes (not shown), we have  $\tilde{n}^+(\omega) = \tilde{n}_{\text{NC}}^\pm(\omega)$ , because they are not influenced by the moiré coupling.

Figure 8(a) and (b) summarise the calculated thermal conductivity  $\kappa(T) (= \kappa^+ + \kappa^-)$  of TBG and t-G/hBN, respectively. In each figure, the left panel shows a log-log plot of  $\kappa(T)$  for  $2 < T < 100$  K. Here the vertical axis is scaled by the constant mean-free-path length  $\Lambda$ , which is assumed to be independent of temperature. The colored lines correspond to different twist angles. The black-dashed line represents the non-coupled bilayer case,  $\kappa_{\text{NC}}$ , which is proportional to  $T^2$  as given in Eq. (24). Here, we find that thermal conductivity is suppressed from the non-coupled case, notably around 20 K, while it converges towards the non-coupled value as increasing temperatures.

To better understand the change from the intrinsic graphene, we plot the relative thermal conductivity,  $\kappa(T)/\kappa_{\text{NC}}(T)$ , in the right panel of Fig. 8(a) and (b). Here, suppression of thermal conductivity is represented

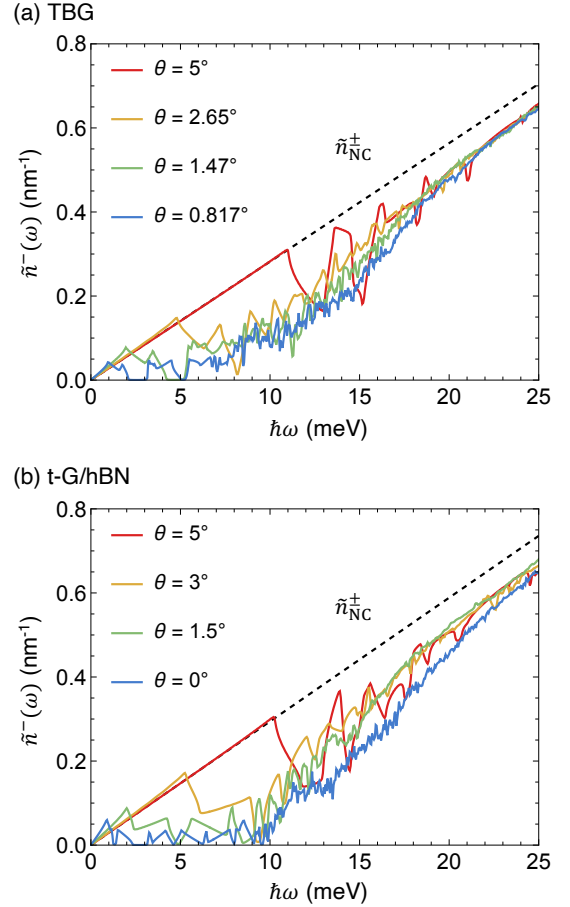


Figure 7. (a) Velocity-weighted density of states (VDOS) of the antisymmetric modes,  $\tilde{n}^-(\omega)$ , in TBGs with various twist angles. Black dashed lines represents  $\tilde{n}_{\text{NC}}^+ = \tilde{n}_{\text{NC}}^-$  for a non-coupled bilayer [Eq. (23)]. The VDOS for symmetric phonons  $\tilde{n}^+$  is equal to  $\tilde{n}_{\text{NC}}^\pm$ . (b) Similar plots for t-G/hBN.

by a value below unity. We can see that the suppression occurs over a wide temperature range except near the low-temperature limit. This suppression becomes more pronounced as the twist angle is smaller, where the largest reduction of up to  $\sim 35\%$  for  $0.817^\circ$  TBG and up to  $\sim 40\%$  for  $0^\circ$  t-G/hBN takes place at around 20 K. This can be understood since at around 20 K, heat transport is carried by phonons with energy below  $\sim 20$  meV [see Fig. 4], where the moiré effect on the asymmetric modes are the most notable, as shown by the changes in VDOS [Fig. 7]. There, thermal conductivity is almost entirely came from the symmetric phonon modes,  $\kappa^+ = \kappa_{\text{NC}}/2$  (red-dashed line).

In the zero-temperature limit, we observe that the relative thermal conductivity  $\kappa/\kappa_{\text{NC}}$  rapidly rises and even exceeds 1, indicating that the thermal transport is *enhanced* by the moiré effect. The reason for this phenomenon is explained as follows. Within this temperature range, only phonons in the two lowest moiré phonon bands in  $\omega < \omega_{\text{edge}}$  become relevant in the thermal trans-

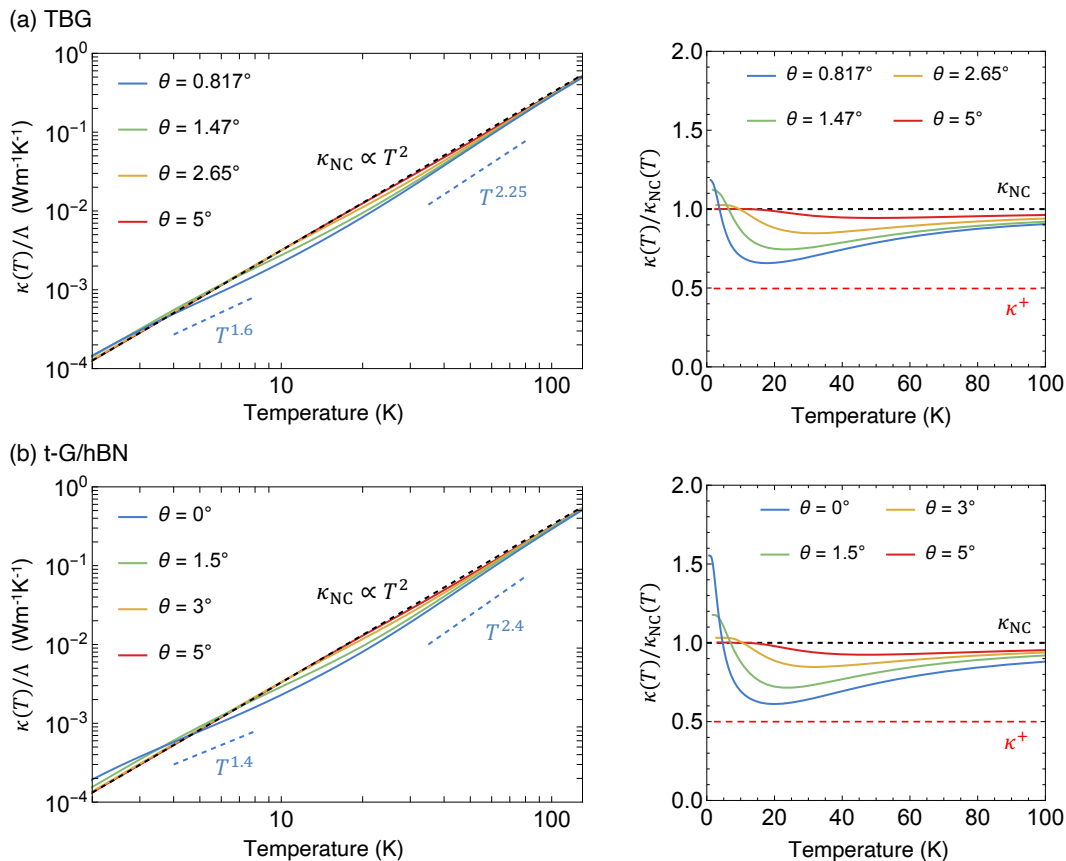


Figure 8. (a) Thermal conductivity in TBGs with various twist angles. The left panel shows the thermal conductivity  $\kappa(T)$  scaled by the mean free path  $\Lambda$ . The right panel shows the relative thermal conductivity to the non-coupled bilayer case,  $\kappa_{\text{NC}}(T)$  [Eq. (24)]. (b) Similar plots for t-G/hBN.

port equation. These phonon modes have a linear dispersion, where the VDOS is given by  $\omega/(2\pi v)$  with the corresponding group velocity  $v$  [Eq. (23) for the noncoupled case]. Since the velocities of the antisymmetric phonon modes are significantly reduced by the moiré effects [see Fig. 5 and Fig. 6], the inverse relation leads to an enhancement of the VDOS, and hence of the thermal conductivity. In decreasing the twist angle, these phonon velocities are monotonically decreased, and eventually converges towards a finite value in the small angle limit [23, 71]. This sets the upper bound of the relative thermal conductivity in the  $T \rightarrow 0$  limit.

We also find that the overall modifications of the thermal conductivity by the moiré effect results in a change of the power coefficient  $\alpha$  in  $\kappa(T) \propto T^\alpha$ , as seen from the logarithmic plot in the left panel of Fig. 8(a) and (b). In the absence of moiré interlayer coupling, thermal conductivity has quadratic temperature dependence ( $\alpha = 2$ ), which comes from the linear dispersion of the original acoustic phonons. However, the enhancement in the low  $T$  limit and the subsequent suppression in higher  $T$  decrease the power coefficient from 2. For example, it is given by  $\alpha \approx 1.6$  in  $0.817^\circ$  TBG and  $\alpha \approx 1.4$  in  $0^\circ$  t-G/hBN within the temperature range of 4 K to 8 K. As

temperature increases further, moiré effect starts to fade out and thermal conductivity returns towards the original value. This requires the power coefficient to be larger than 2. For example, it is given by  $\alpha \approx 2.25$  for  $0.817^\circ$  TBG and  $\alpha \approx 2.4$  for  $0^\circ$  for t-G/hBN which occurs in the range from 35 K to 80 K.

## B. t-MoS<sub>2</sub>

The calculated phonon dispersion for t-MoS<sub>2</sub> is shown in Fig. 9 for both parallel and antiparallel stacking case with twist angle  $0.8^\circ$ . We find that the antisymmetric phonon modes of the parallel-stacked case closely resembles that of TBG [Fig. 5(c)]. This similarity occurs because TBG and t-MoS<sub>2</sub> share triangular domain wall structures [see Fig. 3(a) and (c)]. In an analogous way, the phonon band structure of the antiparallel t-MoS<sub>2</sub> resembles those of t-G/hBN, reflecting a common honeycomb domain-wall structure [Fig. 3(b) and (d)]. This is a natural result because the moiré phonon band structure is qualitatively reproduced by an effective mass-spring model for domain-wall motion [25], and hence it is primarily determined by the geometical structure of domain

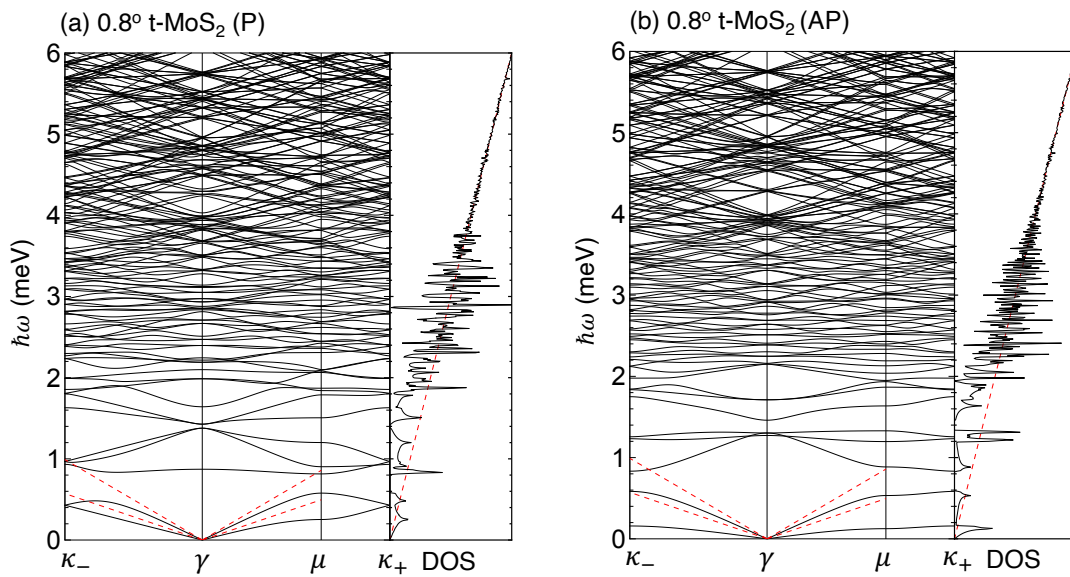


Figure 9. Phonon dispersion and density of states of the antisymmetric modes (black line) and the symmetric modes (red-dashed line) for (a) parallel-stacked (P) and (b) antiparallel-stacked (AP)  $0.8^\circ$  t-MoS<sub>2</sub>.

walls (triangular or honeycomb). We also observe that the characteristic energy scale of the moiré phonon bands in t-MoS<sub>2</sub> is much smaller than in TBG and t-G/hBN, because the original acoustic phonon velocity in MoS<sub>2</sub> is much lower than that of graphene and hBN.

In Fig. 10, we plot the calculated thermal conductivity of t-MoS<sub>2</sub> (P and AP) in a parallel manner to the TBG and t-G/hBN case. Here we find an overall reduction of thermal conductivity and the enhancement near  $T \rightarrow 0$  just as in TBG and t-G/hBN. However, the characteristic temperature range is much lower than TBG and t-G/hBN because of the smaller energy scale of the corresponding moiré phonons. At  $T \sim 4$  K, the thermal conductivity is reduced up to around 35% and 40% in the P and AP cases, respectively. In the limit of  $T \rightarrow 0$ , we find that the AP case exhibits greater enhancement of  $\kappa$  than in the P case. This is attributed to the smaller phonon velocity  $v$  in the lowest branch in the AP case [Fig. 9] and the fact that  $\kappa$  for the linear band regime is proportional to  $1/v$  as argued in the previous section. Accordingly, we have the corresponding change of the power coefficient ( $\alpha$ ) in  $\kappa(T) \propto T^\alpha$  in a similar manner to TBG and t-G/hBN.

#### IV. CONCLUSION

We have studied the thermal transport of various moiré superlattice systems in the low-temperature regime. In general, we found a reduction of thermal conductivity due to an overall flattening of the phonon bands. The largest reduction is around 35-40% which occurs at around 20 K for  $0.817^\circ$  TBG and  $0^\circ$  t-G/hBN and around 4 K for  $0.8^\circ$  t-MoS<sub>2</sub>/MoS<sub>2</sub>. At higher tempera-

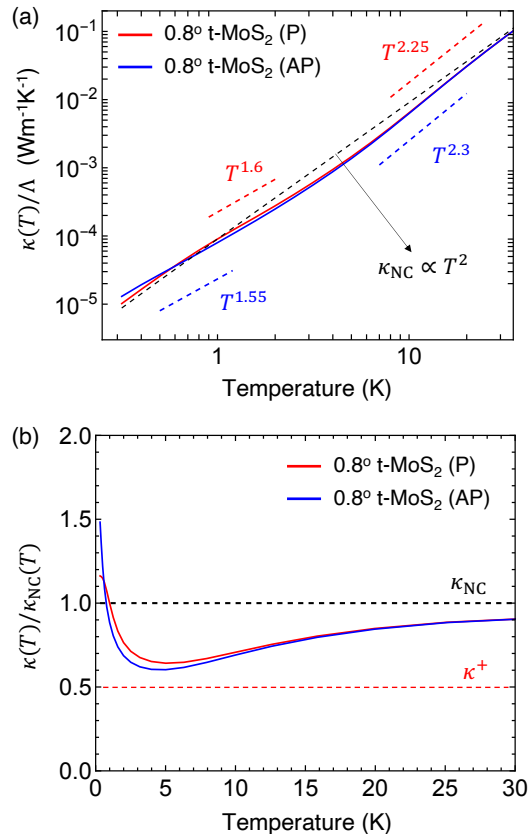


Figure 10. (a) Thermal conductivity of t-MoS<sub>2</sub> with  $\theta = 0.8^\circ$  for the parallel case (red line) and antiparallel case (blue line). (b) Relative thermal conductivity to the noncoupling case,  $\kappa_{\text{NC}}(T)$ .

ture, the thermal conductivity returns towards the original intrinsic value, as the moiré superlattice effect for the acoustic phonons is significant only in the low energy region. These changes result in a characteristic deviation to the original quadratic temperature dependence of two-dimensional systems where linear acoustic phonons dominate the thermal transport properties. The results could provide a pathway for engineering thermal conductivity and observation of the moiré effect in the phonon properties of twisted bilayer system. While the present study is limited in the harmonic approximation, we expect that anharmonic scattering between moiré phonons and the presence of disorder [70, 72] could further de-

crease the thermal conductivity. We leave this imposition for future study.

## ACKNOWLEDGMENTS

This work was supported by JST SPRING, Grant Number JPMJSP2138, JSPS KAKENHI Grants No. JP21H05236, and No. JP21H05232, No. JP20H01840, and by JST CREST Grant No. JPMJCR20T3, Japan.

- 
- [1] C. R. Dean, L. Wang, P. Maher, C. Forsythe, F. Ghahari, Y. Gao, J. Katoch, M. Ishigami, P. Moon, M. Koshino, *et al.*, Hofstadter’s butterfly and the fractal quantum hall effect in moiré superlattices, *Nature* **497**, 598 (2013).
- [2] B. Hunt, J. D. Sanchez-Yamagishi, A. F. Young, M. Yankowitz, B. J. LeRoy, K. Watanabe, T. Taniguchi, P. Moon, M. Koshino, P. Jarillo-Herrero, *et al.*, Massive dirac fermions and hofstadter butterfly in a van der waals heterostructure, *Science* **340**, 1427 (2013).
- [3] Y. Cao, V. Fatemi, A. Demir, S. Fang, S. L. Tomarken, J. Y. Luo, J. D. Sanchez-Yamagishi, K. Watanabe, T. Taniguchi, E. Kaxiras, *et al.*, Correlated insulator behaviour at half-filling in magic-angle graphene superlattices, *Nature* **556**, 80 (2018).
- [4] Y. Cao, V. Fatemi, S. Fang, K. Watanabe, T. Taniguchi, E. Kaxiras, and P. Jarillo-Herrero, Unconventional superconductivity in magic-angle graphene superlattices, *Nature* **556**, 43 (2018).
- [5] A. L. Sharpe, E. J. Fox, A. W. Barnard, J. Finney, K. Watanabe, T. Taniguchi, M. Kastner, and D. Goldhaber-Gordon, Emergent ferromagnetism near three-quarters filling in twisted bilayer graphene, *Science* **365**, 605 (2019).
- [6] H. Polshyn, M. Yankowitz, S. Chen, Y. Zhang, K. Watanabe, T. Taniguchi, C. R. Dean, and A. F. Young, Large linear-in-temperature resistivity in twisted bilayer graphene, *Nature Physics* **15**, 1011 (2019).
- [7] Y. Cao, D. Chowdhury, D. Rodan-Legrain, O. Rubies-Bigorda, K. Watanabe, T. Taniguchi, T. Senthil, and P. Jarillo-Herrero, Strange metal in magic-angle graphene with near planckian dissipation, *Physical review letters* **124**, 076801 (2020).
- [8] J. L. Dos Santos, N. Peres, and A. C. Neto, Graphene bilayer with a twist: Electronic structure, *Physical review letters* **99**, 256802 (2007).
- [9] G. Li, A. Luican, J. Lopes dos Santos, A. Castro Neto, A. Reina, J. Kong, and E. Andrei, Observation of van hove singularities in twisted graphene layers, *Nature physics* **6**, 109 (2010).
- [10] G. Trambly de Laissardière, D. Mayou, and L. Magaud, Localization of dirac electrons in rotated graphene bilayers, *Nano letters* **10**, 804 (2010).
- [11] E. S. Morell, J. Correa, P. Vargas, M. Pacheco, and Z. Barticevic, Flat bands in slightly twisted bilayer graphene: Tight-binding calculations, *Physical Review B* **82**, 121407 (2010).
- [12] A. Luican, G. Li, A. Reina, J. Kong, R. Nair, K. S. Novoselov, A. K. Geim, and E. Andrei, Single-layer behavior and its breakdown in twisted graphene layers, *Physical review letters* **106**, 126802 (2011).
- [13] R. Bistritzer and A. H. MacDonald, Moiré bands in twisted double-layer graphene, *Proceedings of the National Academy of Sciences* **108**, 12233 (2011).
- [14] P. Moon and M. Koshino, Energy spectrum and quantum hall effect in twisted bilayer graphene, *Physical Review B* **85**, 195458 (2012).
- [15] M. Yankowitz, J. Xue, D. Cormode, J. D. Sanchez-Yamagishi, K. Watanabe, T. Taniguchi, P. Jarillo-Herrero, P. Jacquod, and B. J. LeRoy, Emergence of superlattice dirac points in graphene on hexagonal boron nitride, *Nature physics* **8**, 382 (2012).
- [16] J. Jung, A. M. DaSilva, A. H. MacDonald, and S. Adam, Origin of band gaps in graphene on hexagonal boron nitride, *Nature communications* **6**, 6308 (2015).
- [17] J.-W. Jiang, B.-S. Wang, and T. Rabczuk, Acoustic and breathing phonon modes in bilayer graphene with moiré patterns, *Applied Physics Letters* **101**, 023113 (2012).
- [18] J. Campos-Delgado, L. G. Cançado, C. A. Achete, A. Jorio, and J.-P. Raskin, Raman scattering study of the phonon dispersion in twisted bilayer graphene, *Nano Research* **6**, 269 (2013).
- [19] A. I. Cocemasov, D. L. Nika, and A. A. Balandin, Phonons in twisted bilayer graphene, *Physical Review B* **88**, 035428 (2013).
- [20] Y. W. Choi and H. J. Choi, Strong electron-phonon coupling, electron-hole asymmetry, and nonadiabaticity in magic-angle twisted bilayer graphene, *Physical Review B* **98**, 241412 (2018).
- [21] M.-L. Lin, Q.-H. Tan, J.-B. Wu, X.-S. Chen, J.-H. Wang, Y.-H. Pan, X. Zhang, X. Cong, J. Zhang, W. Ji, *et al.*, Moiré phonons in twisted bilayer mos<sub>2</sub>, *Acs Nano* **12**, 8770 (2018).
- [22] P. Parzefall, J. Holler, M. Scheuck, A. Beer, K.-Q. Lin, B. Peng, B. Monserrat, P. Nagler, M. Kempf, T. Korn, and C. Schüller, Moiré phonons in twisted mose<sub>2</sub>-wse<sub>2</sub> heterobilayers and their correlation with interlayer excitons, *2D Materials* **8**, 035030 (2021).
- [23] M. Koshino and Y.-W. Son, Moiré phonons in twisted bilayer graphene, *Physical Review B* **100**, 075416 (2019).

- [24] N. Suri, C. Wang, Y. Zhang, and D. Xiao, Chiral phonons in moiré superlattices, *Nano Letters* **21**, 10026 (2021), 2108.13000.
- [25] L. P. Krisna and M. Koshino, Moiré phonons in graphene/hexagonal boron nitride moiré superlattice, *Physical Review B* **107**, 115301 (2023).
- [26] M. Lamparski, B. V. Troeye, and V. Meunier, Soliton signature in the phonon spectrum of twisted bilayer graphene, *2D Materials* **7**, 025050 (2020).
- [27] I. Maity, M. H. Naik, P. K. Maiti, H. R. Krishnamurthy, and M. Jain, Phonons in twisted transition-metal dichalcogenide bilayers: Ultrasoft phasons and a transition from a superlubric to a pinned phase, *Physical Review Research* **2**, 013335 (2020).
- [28] A. C. Gadelha, D. A. A. Ohlberg, C. Rabelo, E. G. S. Neto, T. L. Vasconcelos, J. L. Campos, J. S. Lemos, V. Ornelas, D. Miranda, R. Nadas, F. C. Santana, K. Watanabe, T. Taniguchi, B. van Troeye, M. Lamparski, V. Meunier, V.-H. Nguyen, D. Paszko, J.-C. Charlier, L. C. Campos, L. G. Cançado, G. Medeiros-Ribeiro, and A. Jorio, Localization of lattice dynamics in low-angle twisted bilayer graphene, *Nature* **590**, 405 (2021).
- [29] J. Quan, L. Linhart, M.-L. Lin, D. Lee, J. Zhu, C.-Y. Wang, W.-T. Hsu, J. Choi, J. Embley, C. Young, T. Taniguchi, K. Watanabe, C.-K. Shih, K. Lai, A. H. MacDonald, P.-H. Tan, F. Libisch, and X. Li, Phonon renormalization in reconstructed MoS<sub>2</sub> moiré superlattices, *Nature Materials* **20**, 1100 (2021).
- [30] I. Maity, A. A. Mostofi, and J. Lischner, Chiral valley phonons and flat phonon bands in moiré materials, *Physical Review B* **105**, l041408 (2022), 2108.03965.
- [31] J. Z. Lu, Z. Zhu, M. Angeli, D. T. Larson, and E. Kaxiras, Low-energy moiré phonons in twisted bilayer van der Waals heterostructures, *Physical Review B* **106**, 144305 (2022).
- [32] B. Xie and J. Liu, Lattice distortions, moiré phonons, and relaxed electronic band structures in magic-angle twisted bilayer graphene, *Physical Review B* **108**, 094115 (2023).
- [33] N. Giroto, L. Linhart, and F. Libisch, Coupled phonons in twisted bilayer graphene, *Physical Review B* **108**, 155415 (2023).
- [34] A. A. Balandin, S. Ghosh, W. Bao, I. Calizo, D. Teweldebrhan, F. Miao, and C. N. Lau, Superior thermal conductivity of single-layer graphene, *Nano letters* **8**, 902 (2008).
- [35] D. Ghosh, I. Calizo, D. Teweldebrhan, E. P. Pokatilov, D. L. Nika, A. A. Balandin, W. Bao, F. Miao, and C. N. Lau, Extremely high thermal conductivity of graphene: Prospects for thermal management applications in nanoelectronic circuits, *Applied Physics Letters* **92**, 151911 (2008).
- [36] W. Cai, A. L. Moore, Y. Zhu, X. Li, S. Chen, L. Shi, and R. S. Ruoff, Thermal transport in suspended and supported monolayer graphene grown by chemical vapor deposition, *Nano letters* **10**, 1645 (2010).
- [37] S. Chen, Q. Wu, C. Mishra, J. Kang, H. Zhang, K. Cho, W. Cai, A. A. Balandin, and R. S. Ruoff, Thermal conductivity of isotopically modified graphene, *Nature materials* **11**, 203 (2012).
- [38] J. H. Seol, I. Jo, A. L. Moore, L. Lindsay, Z. H. Aitken, M. T. Pettes, X. Li, Z. Yao, R. Huang, D. Broido, *et al.*, Two-dimensional phonon transport in supported graphene, *Science* **328**, 213 (2010).
- [39] S. Ghosh, W. Bao, D. L. Nika, S. Subrina, E. P. Pokatilov, C. N. Lau, and A. A. Balandin, Dimensional crossover of thermal transport in few-layer graphene, *Nature Materials* **9**, 555 (2010).
- [40] Z.-X. Guo, D. Zhang, and X.-G. Gong, Manipulating thermal conductivity through substrate coupling, *Physical Review B* **84**, 075470 (2011).
- [41] L. Lindsay, D. A. Broido, and N. Mingo, Flexural phonons and thermal transport in multilayer graphene and graphite, *Physical Review B* **83**, 235428 (2011).
- [42] A. J. Pak and G. S. Hwang, Theoretical analysis of thermal transport in graphene supported on hexagonal boron nitride: the importance of strong adhesion due to  $\pi$ -bond polarization, *Physical Review Applied* **6**, 034015 (2016).
- [43] J.-H. Zou and B.-Y. Cao, Phonon thermal properties of graphene on h-bn from molecular dynamics simulations, *Applied Physics Letters* **110**, 103106 (2017).
- [44] J.-H. Zou, X.-T. Xu, and B.-Y. Cao, Size-dependent mode contributions to the thermal transport of suspended and supported graphene, *Applied Physics Letters* **115**, 123105 (2019).
- [45] H. Li, H. Ying, X. Chen, D. L. Nika, A. I. Cocemasov, W. Cai, A. A. Balandin, and S. Chen, Thermal conductivity of twisted bilayer graphene, *Nanoscale* **6**, 13402 (2014).
- [46] S. Han, X. Nie, S. Gu, W. Liu, L. Chen, H. Ying, L. Wang, Z. Cheng, L. Zhao, and S. Chen, Twist-angle-dependent thermal conduction in single-crystalline bilayer graphene, *Applied Physics Letters* **118**, 193104 (2021).
- [47] C. Li, B. Debnath, X. Tan, S. Su, K. Xu, S. Ge, M. R. Neupane, and R. K. Lake, Commensurate lattice constant dependent thermal conductivity of misoriented bilayer graphene, *Carbon* **138**, 451 (2018).
- [48] X. Nie, L. Zhao, S. Deng, Y. Zhang, and Z. Du, How interlayer twist angles affect in-plane and cross-plane thermal conduction of multilayer graphene: A non-equilibrium molecular dynamics study, *International Journal of Heat and Mass Transfer* **137**, 161 (2019).
- [49] S. Mandal, I. Maity, A. Das, M. Jain, and P. K. Maiti, Tunable lattice thermal conductivity of twisted bilayer mos<sub>2</sub>, *Physical Chemistry Chemical Physics* **24**, 13860 (2022).
- [50] Y. Cheng, Z. Fan, T. Zhang, M. Nomura, S. Volz, G. Zhu, B. Li, and S. Xiong, Magic angle in thermal conductivity of twisted bilayer graphene, *Materials Today Physics* , 101093 (2023).
- [51] S. Ahmed, S. Alam, and A. Jain, Understanding phonon thermal transport in twisted bilayer graphene, *Physical Review B* **108**, 235202 (2023).
- [52] R. Samajdar, Y. Teng, and M. S. Scheurer, Moiré phonons and impact of electronic symmetry breaking in twisted trilayer graphene, *Physical Review B* **106**, L201403 (2022).
- [53] A. M. Popov, I. V. Lebedeva, A. A. Knizhnik, Y. E. Lozovik, and B. V. Potapkin, Commensurate-incommensurate phase transition in bilayer graphene, *Physical Review B* **84**, 045404 (2011), 1108.2254.
- [54] I. V. Lebedeva, A. A. Knizhnik, A. M. Popov, Y. E. Lozovik, and B. V. Potapkin, Interlayer interaction and relative vibrations of bilayer graphene, *Physical Chemistry Chemical Physics* **13**, 5687 (2011).
- [55] P. San-Jose, A. Gutiérrez-Rubio, M. Sturla, and F. Guinea, Spontaneous strains and gap in graphene on boron nitride, *Physical Review B* **90**, 075428 (2014).

- [56] V. Enaldiev, V. Zolyomi, C. Yelgel, S. Magorrian, and V. Fal'Ko, Stacking domains and dislocation networks in marginally twisted bilayers of transition metal dichalcogenides, *Physical review letters* **124**, 206101 (2020).
- [57] A. Weston, Y. Zou, V. Enaldiev, A. Summerfield, N. Clark, V. Zólyomi, A. Graham, C. Yelgel, S. Magorrian, M. Zhou, *et al.*, Atomic reconstruction in twisted bilayers of transition metal dichalcogenides, *Nature Nanotechnology* **15**, 592 (2020).
- [58] H. Suzuura and T. Ando, Phonons and electron-phonon scattering in carbon nanotubes, *Physical review B* **65**, 235412 (2002).
- [59] N. N. Nam and M. Koshino, Lattice relaxation and energy band modulation in twisted bilayer graphene, *Physical Review B* **96**, 075311 (2017).
- [60] K. Zakharchenko, M. Katsnelson, and A. Fasolino, Finite temperature lattice properties of graphene beyond the quasiharmonic approximation, *Physical review letters* **102**, 046808 (2009).
- [61] B. Sachs, T. Wehling, M. Katsnelson, and A. Lichtenstein, Adhesion and electronic structure of graphene on hexagonal boron nitride substrates, *Physical Review B* **84**, 195414 (2011), 1105.2379.
- [62] S. Carr, D. Massatt, S. B. Torrisi, P. Cazeaux, M. Luskin, and E. Kaxiras, Relaxation and domain formation in incommensurate two-dimensional heterostructures, *Physical Review B* **98**, 224102 (2018).
- [63] C. Woods, L. Britnell, A. Eckmann, R. Ma, J. Lu, H. Guo, X. Lin, G. Yu, Y. Cao, R. V. Gorbachev, *et al.*, Commensurate–incommensurate transition in graphene on hexagonal boron nitride, *Nature physics* **10**, 451 (2014).
- [64] J. Ziman, *Electrons and Phonons* (Oxford University Press, 2001).
- [65] R. Prasher, Thermal boundary resistance and thermal conductivity of multiwalled carbon nanotubes, *Physical Review B* **77**, 075424 (2008).
- [66] J. Heremans and C. Beetz Jr, Thermal conductivity and thermopower of vapor-grown graphite fibers, *Physical Review B* **32**, 1981 (1985).
- [67] P. Klemens and D. Pedraza, Thermal conductivity of graphite in the basal plane, *Carbon* **32**, 735 (1994).
- [68] A. Uri, S. Grover, Y. Cao, J. A. Crosse, K. Bagani, D. Rodan-Legrain, Y. Myasoedov, K. Watanabe, T. Taniguchi, P. Moon, *et al.*, Mapping the twist-angle disorder and Landau levels in magic-angle graphene, *Nature* **581**, 47 (2020).
- [69] T. Benschop, T. A. de Jong, P. Stepanov, X. Lu, V. Stalman, S. J. van der Molen, D. K. Efetov, and M. P. Allan, Measuring local moiré lattice heterogeneity of twisted bilayer graphene, *Physical Review Research* **3**, 013153 (2021).
- [70] H. Ochoa and R. M. Fernandes, Degradation of phonons in disordered moiré superlattices, *Physical review letters* **128**, 065901 (2022).
- [71] Q. Gao and E. Khalaf, Symmetry origin of lattice vibration modes in twisted multilayer graphene: Phonons versus moiré phonons, *Physical Review B* **106**, 075420 (2022).
- [72] N. Nakatsuji and M. Koshino, Moiré disorder effect in twisted bilayer graphene, *Physical Review B* **105**, 245408 (2022).